An Adaptive Visuomotor Transformation Reservoir Embedded in the Vertebrate Brain

Yu Qian[1,2,4,*], Sha Li[1,3,4], Ming-Chuan Chen[1], Xu-Fei Du[1,*] & Jiu-Lin Du[1,2,3,*]

[1] Institute of Neuroscience, Laboratory of Brain Cognition and Brain-Inspired Intelligence Technology, Center for Excellence in Brain Science and Intelligence Technology, Chinese Academy of Sciences, 320 Yue-Yang Road, Shanghai 200031, China

[2] University of Chinese Academy of Sciences, 19A Yu-Quan Road, Beijing 100049, China

[3] School of Life Science and Technology, ShanghaiTech University, 319 Yue-Yang Road, Shanghai 200031, China

[4] These authors contributed equally.

[*] Correspondence E-mail: forestdu@ion.ac.cn; xufeidu@ion.ac.cn; yqian@ion.ac.cn

Abstract

Adaptive sensorimotor transformation is essential for animal survival in dynamic environments. The optic tectum (OT), homologous to the mammalian superior colliculus, serves as a central hub for visuomotor processing. To elucidate how OT circuits discriminate visual inputs and generate relevant behavior outputs, we leveraged the mesoscopic connectome of zebrafish OT to build a biophysically constrained reservoir computing network that models visuomotor transformations. *In silico* lesion revealed that the accuracy and robustness of sensorimotor outputs are governed by different combinations of tectal interneuron (TIN) subtypes. Furthermore, specific lamina-projecting serotoninergic subsystems distinctly bias network output toward either escape or orienting behaviors via regulating TIN activities. Our findings establish a mesoscopic connectome-based reservoir for vertebrate sensorimotor processing, where TINs control accuracy and robustness, highlighting TINs as a tunable gate and serotoninergic neurons as a context-dependent modulator of behavioral flexibility.

Introduction

Biological neural networks are the result of billions of years of evolutionary "hyperparameter tuning", optimizing the structure and function across generations. Unlike artificial neural networks that requires extensive data and iterative training, biological neural networks are endowed with innate computational capabilities. Even from birth, animals can perform complex, survival-critical behaviors such as threat avoidance, reward seeking with minimal experience[1–4]. These remarkable capabilities stem from hardwired circuit architectures whose core computational principles remain largely undeciphered. Understanding these intrinsic network structures is fundamental to uncovering the biological substrate of intelligence[5].

Vision is a primary sensory modality for animal to interpret dynamic environments. The superior colliculus (SC), an evolutionarily conserved sensorimotor hub[6], that rapidly converts retinotopic visual inputs into appropriate behaviors[7–10]. Prior studies have focused primarily on feedforward input-output pathways, providing limited insight into the local computational mechanisms embedded within the sensorimotor hub[11–15].

Larval zebrafish (*Danio rerio*) provide a unique model system for investigating these questions. Their compact and evolutionarily conserved sensorimotor hub-OT(the homologs of SC), optical transparency, and in particular a complete mesoscopic connectome mapped at single-cell resolution enable a level of structural access unmatched in vertebrate systems[16–20]. Yet despite these advantages, experimental interrogation of tectal circuit logic remains challenging. The extreme diversity and density of tectal neuron types make it physically intractable to selectively manipulate defined subnetworks or to systematically trace causal relationships between structure and function[21,22]. These technical constraints have limited our ability to uncover mechanisms about how neural architecture gives rise to appropriate visuomotor transformations.

Computational modeling offers a complementary approach to overcome these challenges. In particular, biologically constrained spiking neural networks (SNNs) grounded in empirical connectome data provide a powerful platform for mechanistic dissection of circuit dynamics[23]. Unlike abstract artificial networks, these models preserve biologically realistic connectivity patterns, neuron types, and temporal dynamics, allowing precise and scalable *in silico* manipulation of network components. This permits causal exploration of how specific subcircuits contribute to emergent population dynamics and behavior, especially in cases where experimental interventions are not feasible[24]. Furthermore, the reservoir computing framework provides a theoretical bridge between structural connectivity and dynamic computation. Reservoirs with fixed, recurrent connectivity, resembling biological networks, have been shown to perform complex temporal tasks such as memory, pattern separation, and dynamic input mapping[25,26].Importantly, biological reservoirs are not static in function. Rather, their dynamic regimes can be modulated by internal states and neuromodulatory influences, enabling a single circuit to flexibly switch between different computational modes[27]. This balance of innate structure and flexible dynamics is a defining feature of adaptive neural systems, yet remains underexplored in large-scale, biologically realistic models[28].

In this study, we leveraged these insights to reconstruct a biophysically constrained reservoir model using over 2,000 single-cell reconstructions of retinal ganglion cells (RGCs) and tectal neurons (TNs) in larval zebrafish. We implemented this architecture as a SNN to simulate visuomotor transformation and validated its emergent dynamics with *in vivo* calcium imaging data. *In silico* lesion experiments revealed that specific tectal interneuron (TIN) types are critical for preserving visuomotor accuracy and robustness. Then we demonstrated that this tectal-inspired

reservoir outperforms artificial recurrent neural networks in chaotic time-series prediction tasks, such as the Lorenz attractor, underscoring the computational advantages of biologically grounded architectures. Furthermore, we identified lamina-specific neuromodulation by serotoninergic (5-HT) subsystems, which gate tectal network dynamics to enable flexible sensorimotor output. Together, these results highlight a paradigm shift in computational neuroscience – moving beyond abstract models toward biologically realistic simulations that reveal how structural motifs and neuromodulation interact to produce adaptive neural computations.

Results

Identification of tectofugal pathways underlying escape and orienting behaviors

To investigate the intrinsic properties of the tectal network, we focused on two well-characterized premotor targets involved in distinct behaviors as the output of the tectal network: the Mauthner cell (M-cell), which drives rapid escape responses[29–31], and the nucleus of the medial longitudinal fasciculus (nMLF), which is implicated in orienting and postural control[15,32,33](Fig. 1a). Leveraging the mesoscopic connectome of larval zebrafish[16], we systematically analyzed the structural connectivity of the OT with these downstream premotor nuclei.

TNs were classified into two principal types: TINs (also known as periventricular interneurons, PVINs) and tectal projection neurons (TPNs, also referred to as periventricular projection neurons, PVPNs) (Fig. 1b). TINs are largely confined to local intratectal circuits and include both excitatory and inhibitory subtypes (Extended Data Fig. 1b). Inhibitory TINs are thought to mediate lateral inhibition and contribute to visual feature extraction and contrast enhancement. In contrast, TPNs serve as the primary output neurons of the tectum. These neurons are predominantly excitatory and extend long-range projections to downstream premotor and motor-associated brainstem regions (Extended Data Fig. 1a). In addition to TINs and TPNs, two other cell types with somata located within the neuropil (Np) of the OT were identified. The first is the superficial interneuron (SIN), an inhibitory neuron that modulates synaptic input in the superficial tectal layers and is implicated in filtering sensory input[34,35]. The second is the superficial projection neuron (SPN), which typically sends descending projections to the contralateral hemisphere (Extended Data Fig. 1g).

To map input–output relations at synaptic resolution, we used sparse labeling of TNs via UAS:sypb-APEX2-TagRFP plasmid injections to tag presynaptic release sites, enabling

104 morphological reconstruction and polarity inference. Axons and dendrites were algorithmically
105 classified using a machine learning-based pipeline (Methods; Extended Data Fig. 1c). We further
106 inferred putative synaptic connectivity using a columnar distance-based proximity algorithm,
107 assigning connection weights based on the number of closely apposed axon–dendrite contact
108 points falling below a defined distance threshold (Methods; Extended Data Fig. 1d).

109 Using this approach, we identified two distinct subtypes of TPNs based on their preferential
110 connectivity to premotor targets. One subtype projects to the caudal dendritic compartment of the
111 M-cell, which we term TPN-E (Escape-type TPNs), and is thus likely involved in initiating escape
112 responses[29–31] (Fig. 1c, left). The other subtype preferentially innervates the nMLF, which we refer
113 to as TPN-O (Orientation-type TPNs), likely contributing to orienting and posture-related
114 visuomotor transformations[15,32,33] (Fig. 1c, right).

115 **Retinotectal laminar and topographic organization subdivides the tectal neuropil into**
116 **microdomains**

117 To examine the spatial organization of retinal inputs onto tectal projection neurons (TPNs), we
118 sparsely labeled individual retinal ganglion cells (RGCs) by microinjecting the plasmid
119 *UAS:tdTomato-CAAX* into *Tg(Huc:H2b-GCaMP6s);Ki(isl2b:GAL4FF)* embryos. This strategy
120 enabled single-cell resolution reconstructions of RGC morphologies, which we registered to a
121 standardized brain template to produce a population-level retinotectal projection map (Extended
122 Data Fig. 2). Among the 464 reconstructed RGCs, the vast majority projected exclusively to the
123 contralateral OT, while a small minority targeted the contralateral intermediate hypothalamus
124 (Extended Data Fig. 2b, c). Within the OT, RGC axon terminals exhibited precise laminar
125 specificity, forming stereotyped arborization patterns across the tectal Np (Fig. 1d). Most RGCs
126 terminated in superficial layers—specifically, in sublayers 1–6 of the stratum fibrosum et griseum
127 superficiale (SFGS)—whereas a smaller proportion arborized in deeper strata, including the
128 stratum opticum (SO), stratum griseum centrale (SGC), and stratum album centrale (SAC)
129 (Extended Data Fig. 2f, g).

130 Consistent with established principles of retinotopy[15,36,37], the spatial positions of RGC
131 somata within the retina predicted their tectal termination zones. Accordingly, we subdivided the
132 tectal neuropil into four functional microdomains: anterior, posterior, medial, and lateral Np (Fig.
133 1e). Before entering the neuropil, RGC axons diverged into distinct arborization fields (AFs),

134 forming presynaptic terminals within specific laminar compartments. Based on branch
135 morphologies and terminal distributions, we identified nine discrete arborization fields (AF1–
136 AF9), each associated with a subset of retinotectal laminae (Extended Data Fig. 2d, e). Notably,
137 two minor RGC branches with established behavioral functions were observed. One traversed AF7
138 to reach the SO layer, previously associated with high-resolution visual processing during prey
139 detection[17,38]. The other projected via AF9 to the deeper SFGS5–6, SGC, or SAC layers—regions
140 implicated in the encoding of global luminance changes, such as flashes, dimming, or looming
141 stimuli[39,40] (Extended Data Fig. 2f, g). The angular size of stimuli conveyed through this latter
142 pathway is a known determinant for initiating visually evoked escape behaviors.

143 Based on the six laminar strata and four topographic orientations projected from RGCs onto
144 the Np, we subdivided the entire tectal Np into 24 distinct subdomains, each representing a unique
145 retinotectal convergence zone (Figure 1f).

146 **Simplified parallel visuomotor transformation pathways reveal functional segregation of**
147 **escape and orienting circuits**

148 Leveraging the mesoscopic connectome, the visuomotor transformation architecture in the OT was
149 modeled based on anatomical assumptions: RGCs project axons into the neuropil (Np), TINs
150 extend both dendrites and axons within the Np, and TPNs contribute primarily dendritic processes
151 to receive processed information (Extended Data Fig. 1c). Analysis of dendritic distributions for
152 the two identified TPN subtypes, TPN-E and TPN-O, across the 24 previously defined Np
153 subdomains revealed subtype-specific spatial segregation.

154 Several subdomains contained dendrites from only one TPN subtype. For example, the SO-
155 A subdomain was innervated exclusively by TPN-O, whereas SGC-P and SAC/SPV-P
156 subdomains—together referred to as the SGC/SAC-P domain—were selectively targeted by TPN-
157 E dendrites (Fig. 1g, h). Tracing upstream connectivity identified two distinct RGC subtypes with
158 restricted projection fields: one terminating in SGC/SAC-P, the other in SO-A (Fig. 1i, j). Synaptic
159 connectivity analysis confirmed this segregation: RGCs projecting to SGC/SAC-P were connected
160 almost exclusively to TPN-E, while those projecting to SO-A selectively innervated TPN-O (Fig.
161 1k).

162 Downstream connectivity further supported this parallel organization. TPN-E projects
163 selectively to the M-cell, whereas TPN-O targets the nMLF (Fig. 1l). Together, these connections

delineate two anatomically and functionally distinct visuomotor transformation pathways. This modular and topographically organized circuit structure suggests that discrete tectal microcircuits transform specific retinal inputs into behaviorally relevant outputs. Furthermore, the observed anterior–posterior segregation is consistent with prior findings[15,39,41–44] that posterior OT domains are preferentially involved in threat-evoked escape responses, whereas anterior regions support prey detection and orienting, reflecting the evolutionary compartmentalization of visuomotor processing in the vertebrate midbrain.

Simulation of tectal visuomotor transformation using SNN

The OT contains diverse TNs with distinct morphologies and distributions, forming a recurrent network capable of complex sensory integration and motor output selection. To investigate the computational roles of different TN subtypes in visuomotor transformation, a SNN was implemented using leaky integrate-and-fire (LIF) neuron models (see Methods).

To assess the validity of the model, initial simulations focused on the simplified parallel visuomotor transformation pathways described earlier. Brief current pulses (25 mV, 100 ms) were injected into either SO-A-projecting RGCs or SGC/SAC-P-projecting RGCs (Fig. 2a). Selective activation of the SO-A RGC population elicited strong spiking responses in TPN-O neurons, but failed to activate TPN-E (Fig. 2b). Conversely, stimulation of SGC/SAC-P RGCs robustly activated TPN-E while leaving TPN-O largely unresponsive (Fig. 2c).

This input specificity was preserved at the premotor level. Stimulation of the SGC/SAC-P pathway led to reliable activation of the M-cell. In contrast, SO-A pathway activation selectively recruited nMLF neurons (Fig. 2d). These simulations confirm that the modeled SNN recapitulates key anatomical and functional features of parallel tectal circuits and reliably transforms visual input patterns into subtype-specific motor-related outputs. This framework provides a mechanistic foundation for dissecting circuit-level computations underlying visuomotor behaviors in the vertebrate midbrain.

***In silico* ablation reveals TIN types contributing to visuomotor transformation accuracy**

Natural visual scenes contain rich spatiotemporal dynamics, requiring coordinated input from diverse RGC subtypes tuned to specific visual features. To provide realistic input to the tectal model, in vivo calcium imaging was performed under monocular visual stimulation. Zebrafish

193 larvae were immobilized in low-melting-point agarose, and stimuli were projected onto a screen
194 contralateral to the recorded OT (Fig. 2f). Three behaviorally relevant stimuli were used: a small
195 moving dot (SMD) representing prey-like motion, a neutral large moving dot (BMD), and a
196 looming stimulus associated with threat detection. Calcium activity in the contralateral tectal Np
197 was recorded across multiple layers and converted to estimate firing rates (see Methods). These
198 time-varying inputs were fed into the SNN, which incorporated excitatory and inhibitory TINs
199 forming a recurrent reservoir within the Np (Fig. 2g).

200 Under intact conditions, the model exhibited accurate and stimulus-specific visuomotor
201 transformation without the need for training. SMD selectively activated TPN-O, while looming
202 stimuli robustly engaged TPN-E, consistent with their respective downstream targets—nMLF for
203 orienting and M-cell for escape behavior. However, in silico ablation of the TIN reservoir
204 profoundly disrupted these dynamics. Network activity became pathologically elevated, and both
205 TPN-O and TPN-E were coactivated in response to all stimulus types, indicating a loss of stimulus
206 discrimination (Fig. 2h).

207 To quantify this disruption, incorrect TPN activations—e.g., TPN-E activation during SMD
208 or TPN-O during looming—were classified as computational errors. Following TIN ablation, error
209 rates significantly increased, reflecting a marked decline in the accuracy of visuomotor
210 transformation (Fig. 2i). To dissect the contributions of individual TIN subtypes, targeted *in silico*
211 ablations were performed by selectively zeroing connection weights from specific TIN
212 morphologies in the connectome matrix (Fig. 2j). Among the various TIN subtypes (Extended Fig.
213 1h–j), the most profound deficits in visuomotor accuracy occurred when inhibitory bistratified
214 TINs targeting both SFGS1-2 and SFGS5-6 (I_SFGS1-2_SFGS5-6; 21.1% accuracy reduction on
215 average) were ablated, followed by the inhibitory non-stratified TINs (I_ns; 14.9% accuracy
216 reduction on average) (Fig. 2k).

217 These findings demonstrate that TINs are essential for constraining tectal network activity,
218 stabilizing recurrent dynamics, and ensuring population-level selectivity. Morphologically distinct
219 inhibitory TINs play critical roles in shaping stimulus-specific outputs, enabling accurate
220 visuomotor transformations from naturalistic inputs. This highlights the functional importance of
221 intratectal processing in mediating behaviorally relevant decisions.

222 ***In silico* ablation reveals TIN types contributing to network robustness**

Robustness to sensory noise is a hallmark of biological neural networks, enabling reliable behavior in unpredictable environments. To investigate the role of specific TIN subtypes in promoting robustness, a combination of behavioral and imaging experiments was performed using noisy visual stimuli. First, behavioral responses were recorded in freely swimming zebrafish exposed to looming stimuli embedded with varying levels of spatiotemporal noise (Fig. 3a). Escape probabilities were quantified using infrared video tracking. Subsequently, the same fish were immobilized for two-photon calcium imaging, allowing direct measurement of RGC activity in response to the same noisy stimuli (Fig. 3b). Using SGC-layer-projecting RGCs (SGC-RGCs) as a representative population, calcium signals revealed a gradual reduction in signal-to-noise ratio as stimulus noise density increased (Fig. 3b, c).

These empirical input patterns were then used to drive the computational SNN model. Looming stimuli with increasing noise levels were fed into the network, and escape probabilities were inferred from M-cell activity (Fig. 3d). Both the real zebrafish and the intact model exhibited notable robustness, maintaining high escape probabilities at low noise levels ($\rho < 0.5$). However, TIN network reshuffling or complete removal significantly impaired both response accuracy and robustness (Fig. 3e). To pinpoint which TIN subtypes are critical for maintaining robustness, targeted in silico ablation was performed at a representative noise level ($\rho = 0.5$). Among all TIN morphologies tested, the inhibitory non-stratified subtype (I_ns) exhibited the strongest impact, with a mean normalized reduction in escape probability of 13.15%. This was followed by bistratified inhibitory TINs projecting exclusively to the SGC and SAC layers (I_SGC_SAC), which produced an 11.23% average reduction in escape probability (Fig. 3f)..

These results demonstrate that distinct TIN morphotypes contribute differentially to the network's resilience against noisy input. Specifically, I_ns and I_SGC_SAC neurons appear to play stronger roles in maintaining decision fidelity under suboptimal sensory conditions, highlighting the functional diversity of intratectal interneurons in promoting behavioral robustness.

TIN reservoir exhibits robust generalization on Lorenz sequence denoising

To evaluate whether the robustness observed in the TIN reservoir extends beyond biologically inspired tasks and generalizes to machine learning domains, we employed the Lorenz chaotic time series—a standard benchmark in nonlinear dynamics and temporal prediction. This system is highly sensitive to initial conditions, such that even small perturbations can result in large

deviations over time, making it an ideal testbed for assessing noise tolerance and predictive stability. Noisy variants of the Lorenz sequence were generated by adding Gaussian noise of varying standard deviations (SD) and were used as input to the TIN reservoir model. In this setup, only the output weights (from reservoir to readout) were trained, while all internal weights remained fixed—analogous to standard reservoir computing frameworks (Fig. 3g). The goal was to reconstruct the clean Lorenz trajectory from the corrupted input.

Despite the high sensitivity of the chaotic sequence, the TIN reservoir consistently demonstrated strong denoising capabilities across noise levels. The output closely tracked the ground truth trajectory, even under moderate perturbations (Fig. 3h). Quantitative comparisons revealed that under low-noise conditions (SD ≤ 0.1), the TIN reservoir outperformed conventional recurrent neural networks (RNN), long short-term memory networks (LSTM), and gated recurrent units (GRU) of equivalent size in terms of predictive accuracy (Fig. 3i). Additionally, the TIN reservoir exhibited lower prediction error variance, further highlighting its noise robustness (Fig. 3j).

These results indicate that the structured recurrent dynamics of the TIN reservoir confer not only biological plausibility but also computational advantages in machine learning contexts. Specifically, its inherent ability to filter noise and preserve temporal information makes it a promising candidate for robust time-series modeling in both neuroscience and artificial intelligence applications.

Discrete serotonergic subsystems differentially modulate tectal output pathways to endow behavioral flexibility

In large-scale neural networks such as OT, which contains over 20,000 neurons and occupies more than one-fifth of the larval zebrafish brain volume. Behavioral fine-tuning through slow synaptic plasticity mechanisms (e.g., STDP, Hebbian learning, LTP, or LTD) is metabolically costly and temporally inefficient. Instead, fast-acting neuromodulatory systems have evolved to flexibly reconfigure circuit dynamics in a context-dependent manner[45–47], enabling adaptive behavioral outputs with minimal rewiring. Among these, the serotonergic (5-HT) system is a phylogenetically conserved monoaminergic pathway implicated in emotions, sleep-wake, learning and memory, reward and punishment modulation [48–54].In mammals, serotonergic projections directly innervate the superior colliculus[55,56], suggesting the candidate role in SC computation.

To investigate whether the 5-HT system directly shape tectal (SC) computations, we leveraged a comprehensive anatomical atlas and identified 5-HT neurons projecting to the OT neuropil(Fig. 4a, left). Serotonergic axons exhibited pronounced laminar specificity, targeting both superficial layers (SO) and deeper layers (SFGS 5–6 and SGC)—layers previously associated with distinct visual feature processing[37] (Fig. 4a, right). Based on axonal projection patterns, we identified two subtypes of 5-HT neurons: SO-projecting (SO-type) type, which arborizing in superficial layer (Fig. 4b), and SGC-projecting (SGC-type) type targeting deeper layers (Fig. 4c). In addition to their distinct axonal projection patterns, SO-type and SGC-type 5-HT neurons also exhibit significant differences in dendritic architecture. Notably, the dendrites of SGC-type neurons extend deep into the intermediate hypothalamus (Fig. 4c, bottom), suggesting potential regulation by internal states such as hunger or satiety. In vivo calcium imaging during light-dark transitions revealed divergent sensory tuning: SO-type neurons exhibited sustained responses to continuous illumination, consistent with a role in contextual background modulation, whereas SGC-type neurons showed transient responses to luminance changes, suggesting sensitivity to dynamic visual cues (Fig. 4d).

To examine the physiological impact of serotonergic modulation on tectal microcircuits, we performed whole-cell recordings of TINs. Bath application of 10 μM 5-HT significantly increased spontaneous firing rates (Fig. 4e, f), indicating that 5-HT can increase neuronal excitability. Thus, we computationally lowered the firing thresholds of TNs with dendrites in either the SO or SGC layers, to mimicking selective activation of serotonergic subtypes (Fig. 4g) in the spiking neural network (SNN) model. Simulation results revealed that activating the SO-type selectively enhanced TPN-O responses (Fig. 4i, top), whereas SGC-type preferentially increased TPN-E activity (Fig. 4i, bottom) with BMD stimulus input. However, the BMD stimulus that typically engages both output pathways (Fig. 4h). These findings suggest that laminar-selective serotonergic subsystems can dynamically bias tectal output based on contextual demands.

To test the behavioral relevance of this mechanism, we selectively ablated SGC-type 5-HT neurons using targeted two-photon laser ablation in (Fig. 4j). This manipulation significantly impaired looming-evoked escape behaviors in free-swimming zebrafish (Fig. 4k), confirming the critical role of SGC-type serotonergic modulation in threat-driven visuomotor transformation. Collectively, these results demonstrate that discrete serotonergic subsystems, defined by laminar innervation and functional tuning, differentially gate tectal output pathways. Such architecture

enables rapid and flexible reconfiguration of visuomotor responses based on internal states and sensory context, providing an efficient solution for behavioral adaptation in dynamic environments.

Discussion

This study establishes the zebrafish optic tectum (OT) as a biologically grounded reservoir computing network in which the morphological diversity of tectal interneurons (TINs) enables robust visuomotor transformations, and lamina-specific serotonergic modulation dynamically reconfigures output pathways to support behavioral flexibility. By integrating a large-scale mesoscopic connectome with a spiking neural network (SNN) constrained by single-cell morphology and synaptic topography, we provide a mechanistic account of how innate midbrain circuits perform flexible sensorimotor computations without the need for learning.

Our results reveal two principal mechanisms underlying this computation. First, the diversity of stratified inhibitory and excitatory TINs forms a heterogeneous recurrent network that expands the separability of sensory inputs, echoing the high-dimensional projection principle in artificial reservoir networks. This suggests that evolutionary diversification of interneuron morphology serves as a structural solution for enhancing temporal coding and stimulus discrimination[57,58]. Second, we show that serotonergic subsystems projecting to distinct tectal layers act as laminar-specific gain controllers: activating SO-projecting 5-HT neurons biases the network toward orienting behavior, while SGC-projecting 5-HT neurons enhance escape-related outputs. This demonstrates that a conserved anatomical feature—laminar targeting—can be repurposed to implement a form of neuromodulatory multiplexing, allowing the same hardwired circuit to flexibly switch behavioral modes depending on internal state or environmental context[59,60].

In contrast to prior tectal models that emphasized feedforward pathways or abstract dynamics, our reservoir model captures both the structural and functional complexity of the OT, enabling causal dissection of recurrent computations that are otherwise inaccessible to experimental perturbation. Moreover, the model generalizes to artificial tasks—such as Lorenz sequence denoising—outperforming conventional recurrent neural networks in noise-robust prediction. This underscores the computational advantage of biologically evolved network architectures, even outside their native domain[61]. Importantly, our findings also suggest a framework for reinterpreting tectal circuit motifs in terms of computational primitives. For instance, the parallel TPN-E and TPN-O pathways resemble a hardwired “output layer,” while the TIN reservoir transforms

incoming RGC input into a high-dimensional population code that is selectively decoded based on behavioral context. This circuit design enables a form of real-time sensory selection, where behavior-specific outputs are recruited according to both sensory input and neuromodulatory state.

Despite these advances, several key questions remain. One outstanding issue is whether neuromodulators beyond serotonin, such as dopamine and norepinephrine, exhibit similarly stratified targeting in the OT and how these systems interact to coordinate flexible sensorimotor control[62,63]. Another question concerns the role of synaptic plasticity in shaping or refining tectal computations: while our model operates with fixed connectivity, experience-dependent modifications may adjust reservoir dynamics over longer timescales[64]. Additionally, it remains unknown how this tectal reservoir interacts with other midbrain and hindbrain structures to coordinate distributed sensorimotor transformations—a question that will require multi-region imaging and perturbation in freely behaving animals.

Finally, our work raises intriguing developmental questions: How do such precise morphologies and laminar targeting rules arise during circuit assembly? Do different TIN subtypes follow distinct genetic programs or activity-dependent cues? Addressing these issues could provide fundamental insights into how evolution sculpts flexible yet robust neural systems through constrained developmental rules.

In sum, our study offers a biologically grounded computational framework that unifies structural connectivity, interneuron diversity, and neuromodulation into a coherent model of real-time sensorimotor processing. These findings underscore that biological structure is not merely descriptive—it is fundamentally computational. By embracing this principle, we may uncover generalizable algorithms from the brain's architecture to inspire more robust and adaptable artificial intelligence.

367 ## Materials and methods

368 ### Zebrafish husbandry and preparation

369 Zebrafish larvae were maintained under standard conditions at 28.5°C with a 14 h light/10 h dark
370 photoperiod. Larvae were kept in Hank's solution until 2 dpf, after which they were transferred to
371 facility water. Beginning at 5 dpf, larvae were fed rotifers once daily. All experiments were
372 conducted using larvae aged 6–7 dpf.

373 For in vivo imaging experiments, larvae were embedded in 2.0% low-melting-point agarose
374 (Sigma) dissolved in facility water. 5 minutes post-embedding, facility water was added to the
375 recording chamber. For whole-cell recordings, facility water was replaced with an external
376 solution containing (in mM): 134 NaCl, 2.9 KCl, 2.1 $CaCl_2 \cdot 2H_2O$, 1.2 $MgCl_2 \cdot 6H_2O$, 10 HEPES,
377 and 10 D-glucose (pH 7.8, 290 mOsm).

378 ### Zebrafish lines

379 Transgenic zebrafish larvae were in a nacre background[65]. Fishline *Tg(-7atoh7:GAL4-*
380 *VP16)s1992t* (in abbreviation: *Tg(-7atoh7:GAL4-VP16)*)[66],
381 *Tg(UAS:GCaMP6s)nkUAShspzGCaMP6s13a* (*Tg(UAS:GCaMP6s)*)[67],
382 *Tg2(elavl3:GCaMP6s)a13203* (*Tg2(elavl3:GCaMP6s)*)[68] were described in previous studies,
383 respectively.

384 *Tg(dbh:GAL4FF,5×UAS-hsp:Rno.Trpv1-TagRFP)ion88d* (*Tg(dbh:GAL4FF,UAS:Trpv1-*
385 *TagRFP)*) was constructed by Dr. Chang-Mei Zhang at Jiu-Lin Du's laboratory with Tol2 system.
386 *Ki(tph2:GAL4FF,myl7:EGFP)ion127d* (*Ki(tph2:GAL4FF,myl7:EGFP)*)line was constructed by
387 Dr. Fu-Nin Li at Jiu-Lin Du's laboratory with a CRISPR–Cas9-mediated knock-in approach.
388 *Tg(elavl3:Hsa.H2B-GCaMP8f)ion1m* (*Tg(elavl3:Hsa.H2B-GCaMP8f)*) was constructed by Yu
389 Mu's Laboratory.

390 ### SNN construction

391 In this study, we constructed a biologically plausible SNN using BrainPy, a flexible and high-
392 performance simulation framework for spiking dynamics and neural computation[69]. The neuronal
393 units are modeled using the LIF neuron with an absolute refractory period, capturing key temporal
394 dynamics observed in vertebrate neurons.

The subthreshold dynamics of membrane potential $V(t)$ are governed by:

$$\tau \frac{dV(t)}{dt} = -\left(V(t) - V_{\text{rest}}\right) + R_m I_{\text{syn}}(t), \text{for } t \notin \left[t_{\text{spike}}, t_{\text{spike}} + \tau_{\text{ref}}\right]$$

Where $V(t)$ is the membrane potential, V_{rest} is the resting potential, V_{reset} is the reset potential after a spike, V_{th} is the spike threshold, τ is the membrane time constant, τ_{ref} is the refractory period, R_m is the membrane resistance, $I_{\text{syn}}(t)$ is the total synaptic current input.

When $V(t) \geq V_{\text{th}}$, the neuron emits a spike and resets to V_{reset} , remaining inactive for the duration of τ_{ref} . The detailed parameterization for each modeled neuron type is listed in Supplementary Table 1.

Synaptic inputs are modeled using single-exponential decay conductance-based synapses, a commonly used approximation in SNN modeling that assumes rapid neurotransmitter release, diffusion, and receptor dynamics. We included two types of synapses: AMPA (excitatory) synapses with a short decay time constant; GABA (inhibitory) synapses with a longer decay time constant and negative reversal potential. The conductance $g(t)$ of a synapse after a presynaptic spike at time t_k evolves as:

$$g(t) = \bar{g} \sum_k \exp\left(-\frac{t - t_k}{\tau_s}\right) H\left(t - t_k\right)$$

Where $\bar{g}$ is the maximal synaptic conductance, τ_s is the synaptic decay time constant ($\tau_{AMPA} = 5$ ms, $\tau_{GABA} = 10$ ms), t_k is the time of the k-th presynaptic spike, V_{th} is the spike threshold, $H\left(t - t_k\right)$ is the Heaviside step function.

The corresponding differential form is:

$$\frac{dg(t)}{dt} = -\frac{g(t)}{\tau_s} + \bar{g} \sum_k \delta\left(t - t_k\right)$$

The total synaptic current into the postsynaptic neuron is:

$$I_{\text{syn}}(t) = \sum_i g_i(t) \cdot \left(E_i - V(t)\right)$$

Where E_i is the synaptic reversal potential ($E_{AMPA} = 0$ mV, $E_{GABA} = -80$ mV), and $g_i(t)$ is the time-varying conductance of the i-th synapse.

The number of excitatory and inhibitory neurons in the network is scaled according to the anatomically derived neuron counts from each zebrafish brain region. To simulate *in silico* knockout of a specific neuron type, we set the connection probability between the targeted neurons and all other neurons to zero:

$$P_{\text{conn}}(i,j) = \{0, \quad \text{if } i \in \mathcal{K} \qquad \mathcal{K} \qquad), \quad \text{otherwise}]$$

where $P_{\text{conn}}(i,j)$ is the connection probability between presynaptic neuron i and postsynaptic neuron j, $P_{\text{base}}(i,j)$ is the baseline (non-zero) probability determined by the connectome or anatomical prior, and $\mathcal{K}$ is the set of neurons targeted for knockout.

Calcium fluorescence signals to spike trains

To simulate the effect of RGCs' activity, we convert experimentally recorded calcium fluorescence signals into Poisson-distributed spike trains, where the normalized calcium signal determines the instantaneous firing rate. These spike trains are then used as input to downstream neurons in the model:

$$s_i(t) \sim \text{Poisson}(\lambda_i(t)), \quad \lambda_i(t) = \lambda_{\max} \cdot \frac{C_i(t)}{C_{\max}}$$

where $s_i(t)$ is the binary spike train (0 or 1) for upstream neuron i at time t, $\lambda_i(t)$ is the time-varying firing rate, $C_i(t)$ is the calcium signal (e.g., ΔF/F) of neuron i at time t, $C_{\max}$ is the maximum value of $C_i(t)$ over time for normalization, $\lambda_{\max}$ is the maximum firing rate.

TIN reservoir construction and comparative modeling

We constructed a biologically inspired reservoir network using zebrafish TINs, where the connection weights were determined by the estimated number of potential synapses between neurons based on anatomical connectivity. Excitatory neurons were assigned positive weights, while inhibitory neurons were assigned negative weights. To ensure the reservoir dynamics remain in the echo state regime, we constrained the spectral radius $\rho(W)$ of the recurrent weight matrix W to approximately 1:

$$\rho(W) \approx 1$$

For assessing the accuracy and robustness of visual motion transformations, the network is configured with 6 input nodes and 2 output nodes. For benchmarking using the Lorenz attractor sequence, both the input and output dimensions are adjusted to 3, and the system is converted into a standard Echo State Network (ESN) structure for direct comparison with traditional recurrent neural networks.

The ESN update rule is given by:

$$\mathbf{x}(t+1) = f\left(W_{\text{in}}\mathbf{u}(t) + W\mathbf{x}(t) + \mathbf{b}\right), \quad \mathbf{y}(t) = W_{\text{out}}\mathbf{x}(t)$$

where $\mathbf{x}(t)$ is the reservoir state vector, $\mathbf{u}(t)$ is the input vector, $W_{\text{in}}, W, W_{\text{out}}$ are the input, recurrent, and output weight matrices, respectively. $\mathbf{b}$ is the bias term, $f(\cdot)$ is a nonlinear tanh activation function.

The Lorenz system used as a benchmark task is defined by the following set of differential equations:

$$\begin{cases} \dfrac{dx}{dt} = \sigma(y - x) \\ \dfrac{dy}{dt} = x(\rho - z) - y \\ \dfrac{dz}{dt} = xy - \beta z \end{cases}$$

with standard parameters $\sigma = 10$, $\rho = 28$, and $\beta = 8/3$, yielding a chaotic trajectory.

In the visuomotor transformation task, the reservoir performs feedforward processing without weight updates. However, in the Lorenz task, output weights W_{out} are trained using ridge regression (L2-regularized linear regression):

$$W_{\text{out}} = \mathbf{Y}_{\text{target}}\mathbf{X}^{\top}\left(\mathbf{X}\mathbf{X}^{\top} + \alpha I\right)^{-1}$$

where $\mathbf{X}$ is the matrix of reservoir states, $\mathbf{Y}_{\text{target}}$ is the target output, α is the regularization coefficient, I is the identity matrix. For benchmarking, we compared our model with several standard recurrent architectures:

Vanilla RNN:

$$\mathbf{h}_t = \tanh\left(W_{hh}\mathbf{h}_{t-1} + W_{xh}\mathbf{x}_t + \mathbf{b}_h\right), \quad \mathbf{y}_t = W_{hy}\mathbf{h}_t + \mathbf{b}_y$$

LSTM (Long Short-Term Memory)**:**

$$
\begin{aligned}
\mathbf{f}_t &= \sigma\left(W_f \mathbf{x}_t + U_f \mathbf{h}_{t-1} + \mathbf{b}_f\right) \\
\mathbf{i}_t &= \sigma\left(W_i \mathbf{x}_t + U_i \mathbf{h}_{t-1} + \mathbf{b}_i\right) \\
\mathbf{o}_t &= \sigma\left(W_o \mathbf{x}_t + U_o \mathbf{h}_{t-1} + \mathbf{b}_o\right) \\
\tilde{} & \quad W_c \mathbf{x}_t + U_c \mathbf{h}_{t-1} + \mathbf{b}_c\right) \\
\mathbf{c}_t &= \mathbf{f}_t \odot \quad \odot \\
\mathbf{h}_t &= \mathbf{o}_t \odot \quad)
\end{aligned}
$$

GRU (Gated Recurrent Unit):

$$
\begin{aligned}
\mathbf{z}_t &= \sigma\left(W_z \mathbf{x}_t + U_z \mathbf{h}_{t-1} + \mathbf{b}_z\right) \\
\mathbf{r}_t &= \sigma\left(W_r \mathbf{x}_t + U_r \mathbf{h}_{t-1} + \mathbf{b}_r\right) \\
\mathbf{h}_t &= \tanh\left(W_h \mathbf{x}_t + U_h \left(\mathbf{r}_t \odot \quad {}_h\right)\right) \\
\mathbf{h}_t &= \left(1 - \mathbf{z}_t\right) \odot \quad \odot
\end{aligned}
$$

To evaluate the robustness of the reservoir to noisy inputs, we added Gaussian noise to the Lorenz time series. The noise level was controlled by the SD parameter. The noisy input $\mathbf{x}(t)$ is defined as:

$$
\mathbf{x}(t) = \mathbf{x}(t) + \mathcal{N}
$$

where $\mathbf{x}(t)$ is the original Lorenz time series at time t, $\mathcal{N}$ represents zero-mean Gaussian noise with variance σ^2, σ is the standard deviation regulating the noise level.

The dataset was split as follows: The first 15% of the sequence was used as a warm-up period to allow the reservoir dynamics to stabilize; the next 70% was used as the training set; the final 15% was reserved for testing the model's prediction accuracy.

Finally, to quantify model performance, we employed the Lorenz chaotic time series to evaluate the predictive capability of each reservoir configuration. The Mean Squared Error (MSE) between the predicted time series and the ground truth was used as the primary evaluation metric. The MSE is defined as:

$$
\mathrm{MSE} = \frac{1}{T} \sum_{t=1}^{T} \left\| \mathbf{y}_{\text{pred}}(t) - \mathbf{y}_{\text{true}}(t) \right\|^2
$$

where T is the total number of time steps, $\mathbf{y}_{\text{pred}}(t)$ is the predicted output at time t, $\mathbf{y}_{\text{true}}(t)$ is the ground truth at time t, $\|\cdot\|$ denotes the Euclidean norm.

***In vivo* calcium imaging**

Calcium imaging experiments were usually performed under room temperature on an Olympus Fluoview FVMPE-RS Multiphoton Laser Scanning Microscope with a 20X/1.0 NA water-immersion objective, with 4-5 Hz frame rate (Galvano scanning mode). *Tg(-7atoh7:GAL4-VP16);Tg(UAS:GCaMP6s)* for RGC calcium imaging. *Ki(tph2:GAL4FF,myl7:EGFP);Tg(UAS:GCaMP6s)* for serotoninergic fiber calcium imaging. Calcium imaging paired with whole-cell recording experiment was performed under room temperature on an Olympus Fluoview FV3000 Confocal Laser Scanning Microscope with a 20X/1.0 NA water-immersion objective (Resonant scanning mode), with 30-40 Hz frame rate (resonant scanning mode). *Tg(elavl3:Hsa.H2B-GCaMP8f)* for Calcium imaging paired with whole-cell recording experiment. Images with severe drifts were abandoned.

Calcium activity analysis

Images were aligned using the MultiStackReg plugin in ImageJ. Regions of interest (ROIs) were manually defined based on morphology and regional signal activity. Ca^{2+} signals were extracted by the mean gray value of ROI. $\Delta F/F_0$ as computed using a custom MATLAB script, where F0 was calculated by the mean filter of Ca^{2+} signals with the function ordfilt2. Response peak amplitude was defined as the maximum ΔF/F0 within 5 s of stimulus onset, minus the baseline average in the 10 s preceding stimulation. The area under the curve (AUC) was quantified over the 10 s post-stimulus window. Calcium transients exceeding baseline mean ± 2 SD were considered significant events.

Visual stimulation

All stimuli were presented monocularly using a mini-projector positioned lateral to the larva, with a red filter applied to minimize imaging interference.

-Looming stimulus: A black dot expanded at a constant rate on a bright background until filling the visual field over ~3.7 s [70]; 5 trials/fish with 120 s intervals.

Moving-dot stimuli: A black dot moved across a white background. Small and large dots subtended 4° and 16°, respectively, with the same moving velocity; 5 trials/fish with 120 s intervals.

Light–dark stimulation: 1 min of bright illumination (1.23 mW) followed by 1 min of darkness (0.167 mW), repeated three times for a total of 6 min.

***In vivo* electrophysiological recording**

518 Larvae were paralyzed with 100 μg/ml α-bungarotoxin (Sigma) for 10–15 min, then embedded in
519 2% low-melt agarose. In whole-cell recording experiments, micropipettes were filled with internal
520 solution, which consisted of (in mM): 110 K-gluconate, 6 NaCl, 2 MgCl2, 2 CaCl2, 10 HEPES,
521 and 10 EGTA (pH 7.41, 285 mOsm). The calculated chloride reversal potential (E_Cl) was ~−60
522 mV. In whole-cell recording TNs paired calcium response in *Tg(elavl3:Hsa.H2B-GCaMP8f)*,
523 EGTA was replaced with phosphocreatine to avoid calcium chelation. In vivo whole-cell
524 recording of TNs with bath 5-HT solution (dissolved in DMSO, 10mM for stock solution) was
525 performed in wild-type.

526 For in vivo whole-cell recording of TNs, Following paralysis, a small incision was made at
527 the skin between the tectum and hindbrain using a glass pipette (~1 μm tip). After filled with the
528 internal solution, the recording micropipette (20 - 25 MΩ in resistance, 1-mm tip opening) was
529 advanced into the brain through the dissected hole and slowly approached to the TNs with a
530 persistent positive pressure to keep tip clean. After the contact of micropipette tip with TNs
531 membrane, giga-ohm seal was formed by removing the positive pressure and applying a slight
532 negative pressure. Whole-cell recording was achieved by delivering a few brief electrical zaps (50
533 μs to 2 ms) to break the cell membrane beneath the micropipette tip. Recordings were made with
534 a patch-clamp amplifier (MultiClamp 700B, Axon Instruments), and signals were filtered at 5 kHz
535 and sampled at 10 kHz by using Clampex 10.2 (Molecular Devices).

536 **Behavioral assay**

537 Looming-evoked escape responses were captured using a high-speed, infrared-sensitive camera
538 (Redlake Motionscope M3). Each larva was tested in five trials. Escape probability was defined as
539 the number of escape responses across trials. Body posture was quantified using skeletonization
540 algorithms, followed by an angular threshold to detect C-start escape responses[71]. All automated
541 detections were confirmed manually.

542 **Two-photon ablation of SGC-type 5-HT neurons**

543 Two-photon ablations were performed on an Olympus FVMPE-RS multiphoton microscope.
544 SGC-type 5-HT neurons were ablated based on both visual response properties and TagRFP
545 expressed in these neurons in *Tg2(elavl3:GCaMP6s);Ki(tph2:GAL4FF,myl7:EGFP);*
546 *Tg(dbh:GAL4FF,UAS:Trpv1-TagRFP)* larvae. Neurons were ablated by focused 800-nm laser

547 scanning (~2.92 mW) on the soma (~1 μm radius) for 10–12 ms at a constant angular speed.
548 Cellular fragmentation could be observed after successful ablation. Each target was sequentially
549 ablated by manually positioning the ROI on its soma. After ablation, larvae were recovered in
550 facility water for 18–24 h before post-ablation testing.

551 **Acknowledgments**

552 We thank Chao-ming Wang, Tian-qiu Zhang, Si Wu and Yu Mu for their kind support. We
553 appreciate the technical assistance from Hong-Li Wan, Hui Zhang and Qian Hu. We acknowledge
554 the assistance with neuronal morphology registration on the brain template from the Facility of
555 Mapping Brain-wide Mesoscale Connectome at CEBSIT (Institute of Neuroscience) for technical
556 support. This work was supported by National Science and Technology Innovation 2030 Major
557 Program of the Ministry of Science and Technology (2021ZD0204500 and 2021ZD0204502),
558 Science Fund for Creative Research Groups (32321003) and Key Joint Funds for Cooperation
559 (U22B200571) of the National Natural Science Foundation of China, Shanghai Municipal Science
560 and Technology Major Project (18JC1410100 and 2018SHZDZX05), and Key Research Program
561 of Frontier Sciences (QYZDYSSW-SMC028) and Strategic Priority Research Program
562 (XDB32010200) of Chinese Academy of Sciences.

563 **Author contributions**

564 Conceptualization: Y.Q., J.D.; Code writing and brain simulation: Y.Q.; Methodology: Q.Y.;
565 Investigation: Y.Q., S.L., J.D.; Data acquisition and pre-processing of wet experiments (including
566 neuron morphology imaging and reconstruction, calcium imaging, and electrophysiology): S.L.,
567 Q.Y., M.C., X.D.; Funding acquisition: J.D.; Project administration: Y.Q., S.L., J.D.; Supervision:
568 J.D., X.D.; Manuscript writing: Y.Q., S.L., J.D., X.D.

569 **Data availability**

570 Relevant data and codes have been released on GitHub: https://github.com/yqian-
571 CEBSIT/Reservoir-of-Zebrafish-Optic-tectum.

572 **Competing interests**

573 The authors declare no competing financial interests.

References

1. Zador, A. M. A critique of pure learning and what artificial neural networks can learn from animal brains. *Nat. Commun.* **10**, 3770 (2019).
2. Spelke, E. S. & Kinzler, K. D. Core knowledge. *Dev. Sci.* **10**, 89–96 (2007).
3. Hassabis, D., Kumaran, D., Summerfield, C. & Botvinick, M. Neuroscience-Inspired Artificial Intelligence. *Neuron* **95**, 245–258 (2017).
4. He, L. *et al.* Network model with internal complexity bridges artificial intelligence and neuroscience. *Nat. Comput. Sci.* **4**, 584–599 (2024).
5. Luo, L. Architectures of neuronal circuits. *Science* **373**, eabg7285 (2021).
6. Isa, T., Marquez-Legorreta, E., Grillner, S. & Scott, E. K. The tectum/superior colliculus as the vertebrate solution for spatial sensory integration and action. *Curr. Biol.* **31**, R741–R762 (2021).
7. Basso, M. A. & May, P. J. Circuits for Action and Cognition: A View from the Superior Colliculus. *Annu. Rev. Vis. Sci.* **3**, 197–226 (2017).
8. Kardamakis, A. A., Pérez-Fernández, J. & Grillner, S. Spatiotemporal interplay between multisensory excitation and recruited inhibition in the lamprey optic tectum. *eLife* **5**, e16472 (2016).
9. Kardamakis, A. A., Saitoh, K. & Grillner, S. Tectal microcircuit generating visual selection commands on gaze-controlling neurons. *Proc. Natl. Acad. Sci.* **112**, (2015).
10. Suzuki, D. G., Pérez-Fernández, J., Wibble, T., Kardamakis, A. A. & Grillner, S. The role of the optic tectum for visually evoked orienting and evasive movements. *Proc. Natl. Acad. Sci.* **116**, 15272–15281 (2019).

597 11. Naumann, R. K. & Laurent, G. Function and Evolution of the Reptilian Cerebral Cortex. in
598 *Evolutionary Neuroscience* 213–245 (Elsevier, 2020). doi:10.1016/B978-0-12-820584-
599 6.00009-X.
600 12. Wylie, D. R. W., Gutierrez-Ibanez, C., Pakan, J. M. P. & Iwaniuk, A. N. The optic tectum of
601 birds: Mapping our way to understanding visual processing. *Can. J. Exp. Psychol. Rev. Can.*
602 *Psychol. Expérimentale* **63**, 328–338 (2009).
603 13. Cang, J., Savier, E., Barchini, J. & Liu, X. Visual Function, Organization, and Development
604 of the Mouse Superior Colliculus. *Annu. Rev. Vis. Sci.* **4**, 239–262 (2018).
605 14. Robles, E., Laurell, E. & Baier, H. The Retinal Projectome Reveals Brain-Area-Specific
606 Visual Representations Generated by Ganglion Cell Diversity. *Curr. Biol.* **24**, 2085–2096
607 (2014).
608 15. Helmbrecht, T. O., Dal Maschio, M., Donovan, J. C., Koutsouli, S. & Baier, H. Topography
609 of a Visuomotor Transformation. *Neuron* **100**, 1429-1445.e4 (2018).
610 16. Du, X. *et al.* Central nervous system atlas of larval zebrafish constructed using the morphology
611 of single excitatory and inhibitory neurons. *bioRxiv* 2025.06.06.658008 (2025)
612 doi:10.1101/2025.06.06.658008.
613 17. Förster, D. *et al.* Retinotectal circuitry of larval zebrafish is adapted to detection and pursuit
614 of prey. *eLife* **9**, e58596 (2020).
615 18. Simmich, J., Staykov, E. & Scott, E. Zebrafish as an appealing model for optogenetic studies.
616 in *Progress in Brain Research* vol. 196 145–162 (Elsevier, 2012).
617 19. Vanwalleghem, G. C., Ahrens, M. B. & Scott, E. K. Integrative whole-brain neuroscience in
618 larval zebrafish. *Curr. Opin. Neurobiol.* **50**, 136–145 (2018).
619 20. Scott, E. K. The cellular architecture of the larval zebrafish tectum, as revealed by Gal4
620 enhancer trap lines. *Front. Neural Circuits* **3**, (2009).

621 21. Alivisatos, A. P. *et al.* The Brain Activity Map Project and the Challenge of Functional
622 Connectomics. *Neuron* **74**, 970–974 (2012).
623 22. Bauer, A. Q. *et al.* Effective Connectivity Measured Using Optogenetically Evoked
624 Hemodynamic Signals Exhibits Topography Distinct from Resting State Functional
625 Connectivity in the Mouse. *Cereb. Cortex* **28**, 370–386 (2018).
626 23. Sun, Z., Cutsuridis, V., Caiafa, C. F. & Solé-Casals, J. Brain Simulation and Spiking Neural
627 Networks. *Cogn. Comput.* **15**, 1103–1105 (2023).
628 24. Gerstner, W., Sprekeler, H. & Deco, G. Theory and Simulation in Neuroscience. *Science* **338**,
629 60–65 (2012).
630 25. Suárez, L. E. *et al.* Connectome-based reservoir computing with the conn2res toolbox. *Nat.*
631 *Commun.* **15**, 656 (2024).
632 26. Damicelli, F., Hilgetag, C. C. & Goulas, A. Brain connectivity meets reservoir computing.
633 *PLOS Comput. Biol.* **18**, e1010639 (2022).
634 27. Cazettes, F. *et al.* A reservoir of foraging decision variables in the mouse brain. *Nat. Neurosci.*
635 **26**, 840–849 (2023).
636 28. Shine, J. M. Neuromodulatory control of complex adaptive dynamics in the brain. *Interface*
637 *Focus* **13**, 20220079 (2023).
638 29. Temizer, I., Donovan, J. C., Baier, H. & Semmelhack, J. L. A Visual Pathway for Looming-
639 Evoked Escape in Larval Zebrafish. *Curr. Biol.* **25**, 1823–1834 (2015).
640 30. Kohashi, T. & Oda, Y. Initiation of Mauthner- or Non-Mauthner-Mediated Fast Escape
641 Evoked by Different Modes of Sensory Input. *J. Neurosci.* **28**, 10641–10653 (2008).
642 31. Korn, H. & Faber, D. S. The Mauthner Cell Half a Century Later: A Neurobiological Model
643 for Decision-Making? *Neuron* **47**, 13–28 (2005).

644 32. Thiele, T. R., Donovan, J. C. & Baier, H. Descending Control of Swim Posture by a Midbrain
645 Nucleus in Zebrafish. *Neuron* **83**, 679–691 (2014).
646 33. Severi, K. E. *et al.* Neural Control and Modulation of Swimming Speed in the Larval Zebrafish.
647 *Neuron* **83**, 692–707 (2014).
648 34. Baier, H. & Scott, E. K. The Visual Systems of Zebrafish. *Annu. Rev. Neurosci.* **47**, 255–276
649 (2024).
650 35. Abbas, F. & Meyer, M. P. Fish Vision: Size Selectivity in the Zebrafish Retinotectal Pathway.
651 *Curr. Biol.* **24**, R1048–R1050 (2014).
652 36. Kunst, M. *et al.* A Cellular-Resolution Atlas of the Larval Zebrafish Brain. *Neuron* **103**, 21-
653 38.e5 (2019).
654 37. Baier, H. & Scott, E. K. The Visual Systems of Zebrafish. *Annu. Rev. Neurosci.* **47**, 255–276
655 (2024).
656 38. Semmelhack, J. L. *et al.* A dedicated visual pathway for prey detection in larval zebrafish.
657 *eLife* **3**, e04878 (2014).
658 39. Temizer, I., Donovan, J. C., Baier, H. & Semmelhack, J. L. A Visual Pathway for Looming-
659 Evoked Escape in Larval Zebrafish. *Curr. Biol.* **25**, 1823–1834 (2015).
660 40. Dunn, T. W. *et al.* Neural Circuits Underlying Visually Evoked Escapes in Larval Zebrafish.
661 *Neuron* **89**, 613–628 (2016).
662 41. Zhao, P. *et al.* The visuomotor transformations underlying target-directed behavior. *Proc. Natl.*
663 *Acad. Sci.* **122**, e2416215122 (2025).
664 42. Bianco, I. H. & Engert, F. Visuomotor Transformations Underlying Hunting Behavior in
665 Zebrafish. *Curr. Biol.* **25**, 831–846 (2015).
666 43. Fernandes, A. M. *et al.* Neural circuitry for stimulus selection in the zebrafish visual system.
667 *Neuron* **109**, 805-822.e6 (2021).

668 44. Preuss, S. J., Trivedi, C. A., vom Berg-Maurer, C. M., Ryu, S. & Bollmann, J. H. Classification
669 of Object Size in Retinotectal Microcircuits. *Curr. Biol.* **24**, 2376–2385 (2014).
670 45. Bessonova, Y. & Raman, B. Serotonergic amplification of odor-evoked neural responses maps
671 flexibly onto behavioral outcomes.
672 46. Cohn, R., Morantte, I. & Ruta, V. Coordinated and Compartmentalized Neuromodulation
673 Shapes Sensory Processing in Drosophila. *Cell* **163**, 1742–1755 (2015).
674 47. Aston-Jones, G., Rajkowski, J. & Cohen, J. Role of locus coeruleus in attention and behavioral
675 flexibility. *Biol. Psychiatry* **46**, 1309–1320 (1999).
676 48. Marcinkiewcz, C. A. *et al.* Serotonin engages an anxiety and fear-promoting circuit in the
677 extended amygdala. *Nature* **537**, 97–101 (2016).
678 49. Wang, Y. *et al.* Dorsal Raphe Serotonergic Neurons-Ventral Tegmental Area Neural Pathway
679 Promotes Wake From Sleep. *CNS Neurosci. Ther.* **30**, e70141 (2024).
680 50. Oikonomou, G. *et al.* The Serotonergic Raphe Promote Sleep in Zebrafish and Mice. *Neuron*
681 **103**, 686-701.e8 (2019).
682 51. Harkin, E. F., Grossman, C. D., Cohen, J. Y., Béïque, J.-C. & Naud, R. A prospective code for
683 value in the serotonin system. *Nature* (2025) doi:10.1038/s41586-025-08731-7.
684 52. Kawashima, T., Zwart, M. F., Yang, C.-T., Mensh, B. D. & Ahrens, M. B. The Serotonergic
685 System Tracks the Outcomes of Actions to Mediate Short-Term Motor Learning. *Cell* **167**,
686 933-946.e20 (2016).
687 53. Cohen, J. Y., Amoroso, M. W. & Uchida, N. Serotonergic neurons signal reward and
688 punishment on multiple timescales. *eLife* **4**, e06346 (2015).
689 54. Ren, J. *et al.* Anatomically Defined and Functionally Distinct Dorsal Raphe Serotonin Sub-
690 systems. *Cell* **175**, 472-487.e20 (2018).

691 55. Muzerelle, A. Conditional anterograde tracing reveals distinct targeting of individual serotonin
692 cell groups (B5–B9) to the forebrain and brainstem. *Brain Struct Funct* (2016).
693 56. Ren, J. *et al.* Single-cell transcriptomes and whole-brain projections of serotonin neurons in
694 the mouse dorsal and median raphe nuclei. *eLife* **8**, e49424 (2019).
695 57. Buonomano, D. V. & Maass, W. State-dependent computations: spatiotemporal processing in
696 cortical networks. *Nat. Rev. Neurosci.* **10**, 113–125 (2009).
697 58. Maass, W., Natschläger, T. & Markram, H. Real-Time Computing Without Stable States: A
698 New Framework for Neural Computation Based on Perturbations. *Neural Comput.* **14**, 2531–
699 2560 (2002).
700 59. Dayan, P. Twenty-Five Lessons from Computational Neuromodulation. *Neuron* **76**, 240–256
701 (2012).
702 60. Disney, A. A., Aoki, C. & Hawken, M. J. Gain Modulation by Nicotine in Macaque V1.
703 *Neuron* **56**, 701–713 (2007).
704 61. Winnubst, J. *et al.* Reconstruction of 1,000 Projection Neurons Reveals New Cell Types and
705 Organization of Long-Range Connectivity in the Mouse Brain. *Cell* **179**, 268-281.e13 (2019).
706 62. Morilak, D. A. *et al.* Role of brain norepinephrine in the behavioral response to stress. *Prog.*
707 *Neuropsychopharmacol. Biol. Psychiatry* **29**, 1214–1224 (2005).
708 63. Devilbiss, D. M. & Waterhouse, B. D. Phasic and Tonic Patterns of Locus Coeruleus Output
709 Differentially Modulate Sensory Network Function in the Awake Rat. *J. Neurophysiol.* **105**,
710 69–87 (2011).
711 64. Zenke, F., Agnes, E. J. & Gerstner, W. Diverse synaptic plasticity mechanisms orchestrated to
712 form and retrieve memories in spiking neural networks. *Nat. Commun.* **6**, 6922 (2015).

713 65. Lister, J. A., Robertson, C. P., Lepage, T., Johnson, S. L. & Raible, D. W. nacre encodes a
714 zebrafish microphthalmia-related protein that regulates neural-crest-derived pigment cell fate.
715 *Development* **126**, 3757–3767 (1999).
716 66. Del Bene, F. *et al.* Filtering of Visual Information in the Tectum by an Identified Neural Circuit.
717 *Science* **330**, 669–673 (2010).
718 67. Muto, A. *et al.* Activation of the hypothalamic feeding centre upon visual prey detection. *Nat.*
719 *Commun.* **8**, 15029 (2017).
720 68. Kim, D. H. *et al.* Pan-neuronal calcium imaging with cellular resolution in freely swimming
721 zebrafish. *Nat. Methods* **14**, 1107–1114 (2017).
722 69. Wang, C. *et al.* BrainPy, a flexible, integrative, efficient, and extensible framework for
723 general-purpose brain dynamics programming. *eLife* **12**, e86365 (2023).
724 70. Yao, Y. *et al.* Visual Cue-Discriminative Dopaminergic Control of Visuomotor
725 Transformation and Behavior Selection. *Neuron* **89**, 598–612 (2016).
726 71. Dunn, T. W. *et al.* Neural Circuits Underlying Visually Evoked Escapes in Larval Zebrafish.
727 *Neuron* **89**, 613–628 (2016).
728

729 **Figures**

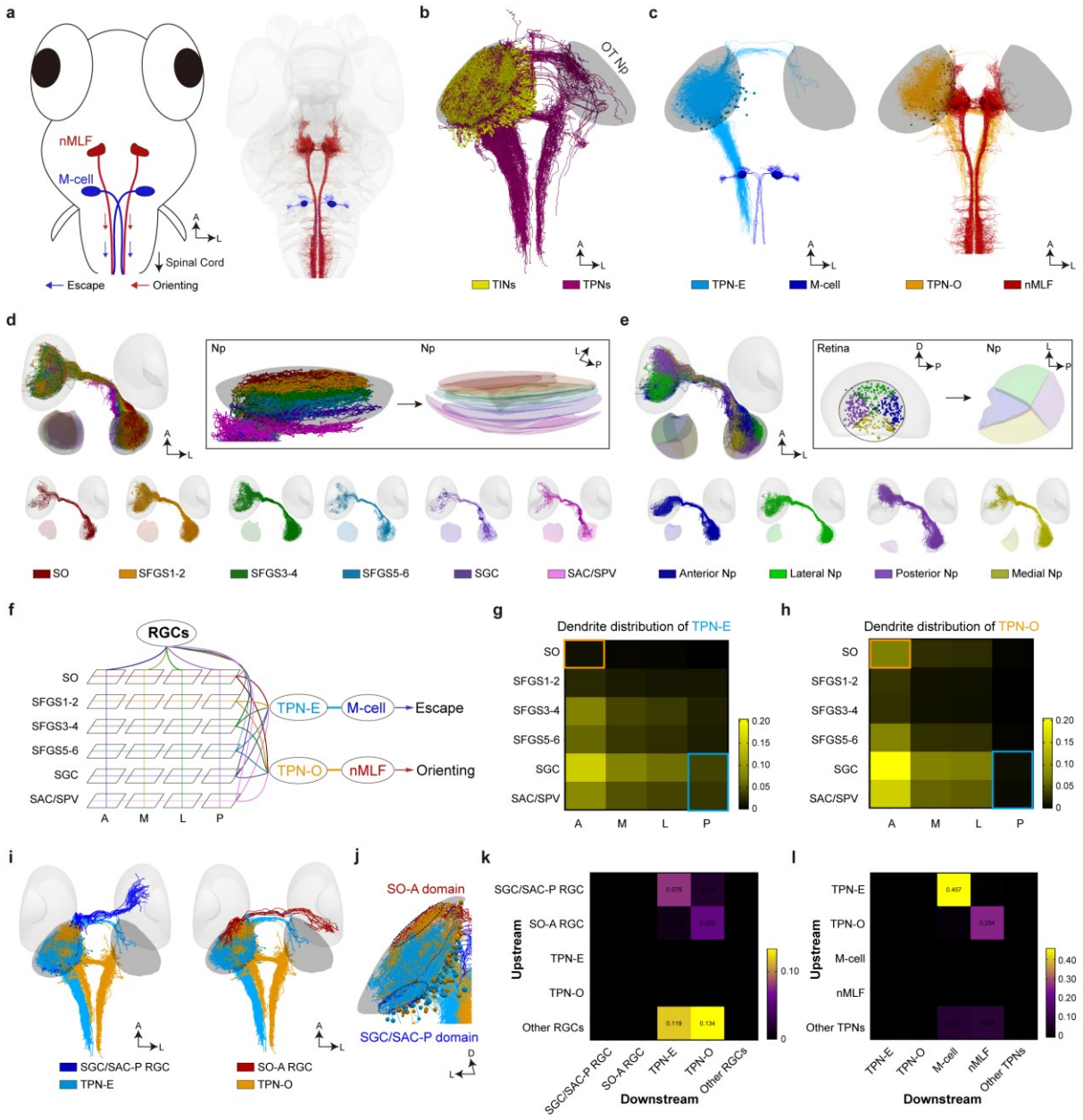

730 **Fig. 1. Anatomical substrates for transforming visual information into escape and orienting**
731 **behaviors in the zebrafish brain.**

732 **a,** Two distinct descending pathways in zebrafish mediating orienting and escape behaviors, driven
733 by premotor neurons in the nucleus of the nMLF and M-cells. Schematic representation (left) and
734 mesoscale connectome structural data demonstrating single-neuron resolution across both
735 pathways (right).

736 **b,** Schematic illustration of the anatomical organization of TINs and TPNs in the OT.
737 **c,** Two distinct subtypes of TPNs exhibiting selective connectivity with either the nucleus of the
738 nMLF or M-cells. Schematic organization of TPN-E subtype exclusively connecting to M-cells
739 (left) and TPN-O subtype showing specific connectivity with nMLF (right).
740 **d,** Lamina-specific retinotectal projections establish six distinct Np strata through retinal RGCs.
741 Stratification progresses from superficial to deep layers: stratum opticum (SO), superficial
742 fibrosum et griseum superficiale sublayers 1-2 (SFGS1-2), SFGS3-4, SFGS5-6, stratum griseum
743 centrale (SGC), and stratum album centrale/stratum periventriculare (SAC/SPV), with individual
744 RGCs projecting exclusively to single laminae.
745 **e,** Topographic organization of retinotectal projections demonstrating spatial inversion along four
746 axes. Anterior-posterior axis: RGCs in the anterior retina projected to posterior Np regions, while
747 posterior retinal RGCs innervated anterior Np regions; Dorsoventral axis: Dorsal retinal RGCs
748 targeted medial Np domains, whereas ventral retinal RGCs terminated in lateral Np domains.
749 **f,** Schematic of visuomotor transformation circuitry. Combinatorial integration of the six-layered
750 stratification (from panel d) and four-column topographic organization (from panel e) within the
751 Np generated 24 functional microdomains. TPN subtypes TPN-E and TPN-O received processed
752 visual signals from distinct Np microdomains, subsequently relaying information to M-cells and
753 the nMLF nucleus, respectively, eliciting escape and orienting behavioral responses.
754 **g,h** Dendritic arborization heatmaps of TPN subtypes TPN-E (g) and TPN-O (h) within the
755 neuropil (Np). Dendritic distribution was quantified by normalizing total branch length per
756 neuronal cluster to maximum projection density (0-1 scale).
757 **i,j** Selective connectivity patterns between RGC subtypes and TPNs. (i) SGC/SAC-P RGCs
758 exhibited preferential connectivity with TPN-E neurons, whereas SO-A RGCs showed stronger
759 anatomical coupling with TPN-O neurons. (j) Coronal view orthogonal to the laminar axis
760 demonstrated enhanced synaptic appositions between SGC/SAC-P RGC terminals and TPN-E
761 dendrites, and between SO-A RGC terminals and TPN-O dendrites, within their respective Np
762 microdomains.
763 **k,l** Connection specificity across neuronal populations. **(**k) SGC/SAC-P RGCs exhibited selective
764 connectivity with TPN-E (connection probability: 7.9%), while SO-A RGCs showed preferential
765 coupling with TPN-O (5.6%). Residual RGCs projecting to other Np microdomains demonstrated
766 no significant connectivity bias. (l) TPN-E neurons formed high-probability synapses with M-cells

767 (45.7%) but not with the nucleus of the nMLF (0.0%), whereas TPN-O neurons preferentially
768 connected to nMLF (25.4%) over M-cells (0.0%, $p<0.001$, χ^2 test).
769

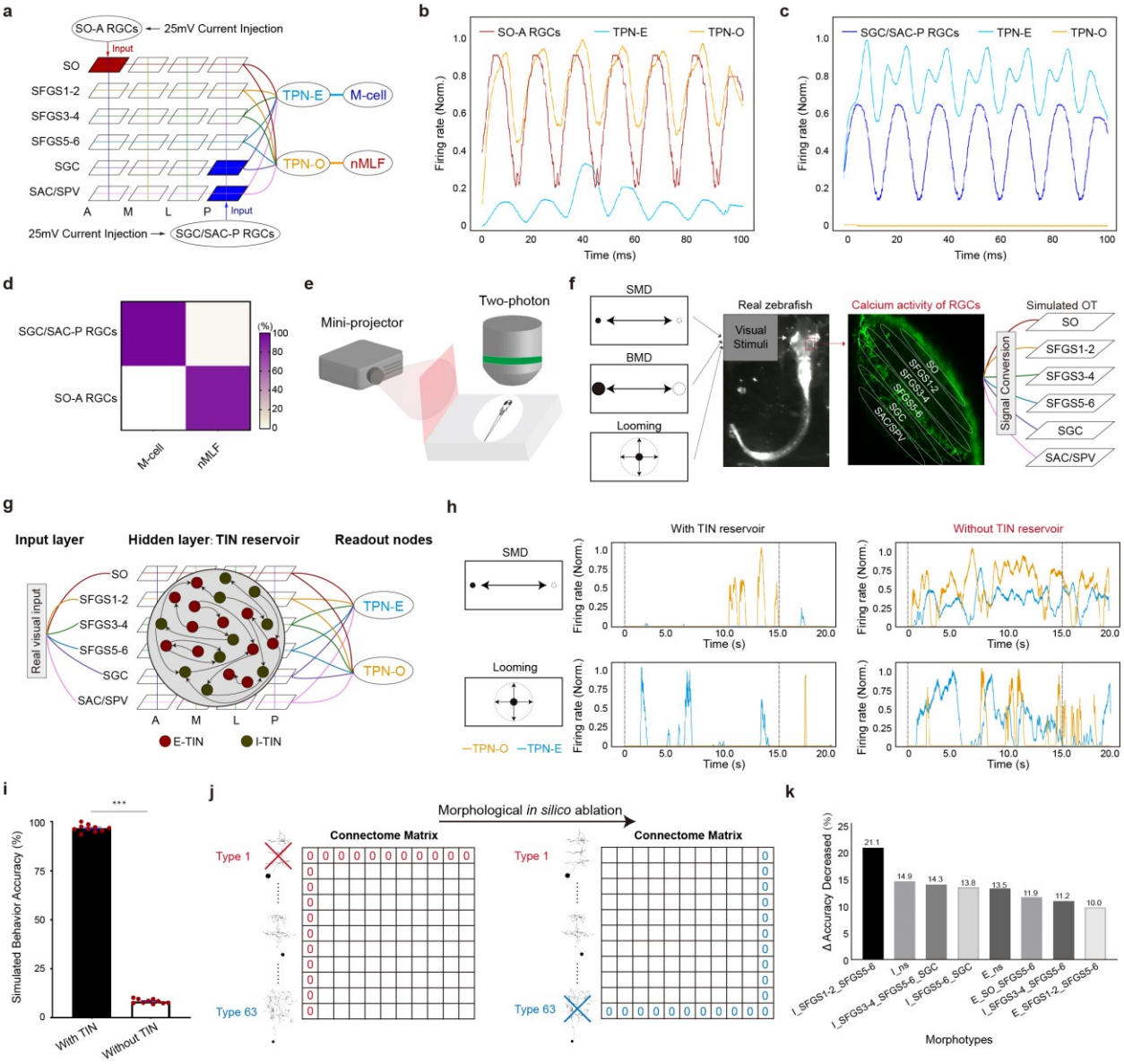

Fig. 2. Computational dissection and morphotype-specific manipulation of visuomotor transformation in the TIN reservoir network.

a, Schematic of selective retinal ganglion cell (RGC) activation via 100-ms intracellular current injection (25 mV): SO-A RGCs (top) and SGC/SAC-P RGCs (bottom).

b,c Activation of SO-A RGCs evoked robust firing in TPN-O neurons (b), whereas SGC/SAC-P RGC stimulation selectively activated TPN-E without eliciting TPN-O responses (c).

d, Mesoscale connectome-based simulations predicting premotor nucleus engagement probability. SGC/SAC-P RGC activation triggered M-cell responses with 99% probability, while SO-A RGC stimulation activated nMLF in 90% of iterations (trials=100)**.**

e, Experimental setup for visual stimulation (projector) and simultaneous two-photon calcium imaging in head-fixed zebrafish.

f, Laminar-specific calcium dynamics in OT Np evoked by three visual stimuli: Small Moving Dot (SMD), Big Moving Dot (BMD), and Looming threat**.**

g, Visuomotor transformation network architecture: Visual inputs processed through E-TIN/I-TIN reservoir with readouts via TPN-E (escape) and TPN-O (orienting) nodes.

h, Firing patterns of TPN-E and TPN-O under SMD (top) /Looming (bottom) stimuli with intact (left) vs. TIN-depleted (right) reservoir (normalized spike rates).

i, TIN-mediated behavioral accuracy enhancement. Correct responses: nMLF activation without M-cell firing during SMD (left); M-cell responses without high-frequency nMLF activity during Looming (right) (Accuracy: 96.7% ± 1.8% with TINs vs. 8.3% ± 1.2% without; $p<0.001$).

j, *In silico* ablation paradigm targeting morphologically defined TIN subtypes in the reservoir network.

k, Top eight TIN subtypes whose ablation maximally impaired visuomotor accuracy. Nomenclature: [E/I][layers][stratification] (e.g., I_SFGS1-2_SFGS5-6: GABAergic bsTINs restricted to SFGS1-2 and SFGS5-6 layers; ns: non-stratified).

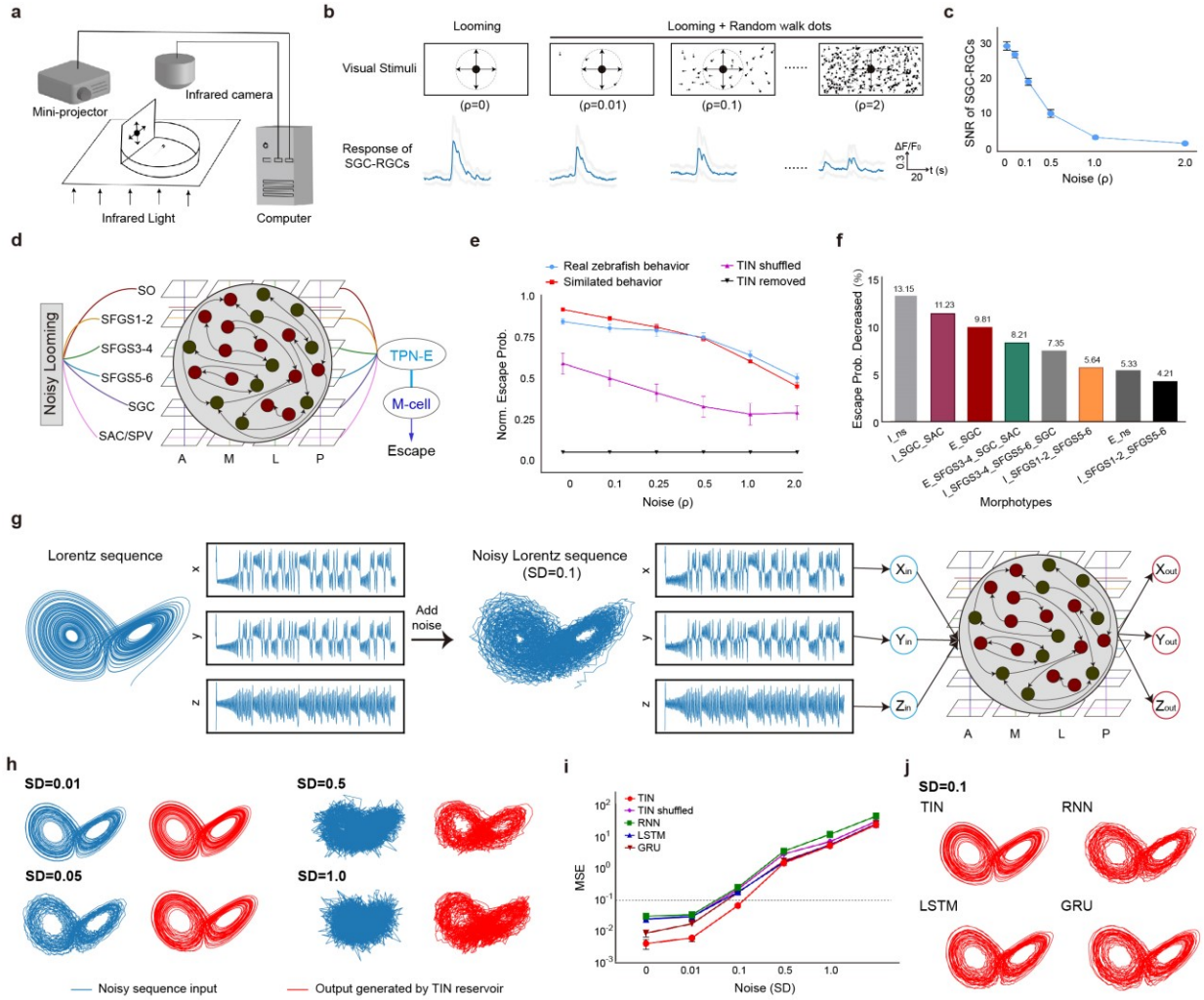

Fig. 3. Neural mechanisms of noise robustness in the visuomotor transformation reservoir

a, Freely swimming assay: visual stimulation with synchronized infrared behavioral recording in zebrafish.

b, Noise-dependent retinal encoding: Top: Looming stimuli with increasing noise density (ρ). Bottom: Corresponding calcium responses of SGC-layer RGCs in OT Np showing signal-to-noise ratio (SNR) degradation (gray lines: SEM, n=5 fish).

c, Quantified noise susceptibility: Inverse correlation between noise density (ρ) and SNR of SGC-RGC responses.

d, TIN reservoir robustness test: Escape probability estimation via M-cell activation to noisy looming stimuli.

e, Noise resilience of behavior.

f, Critical TIN subtypes for robustness: Top 8 morphotypes sustaining escape probability under noise (ρ=0.1).

g, Chaotic signal processing paradigm: Lorenz attractor inputs with additive Gaussian noise processed through TIN reservoir network.

h, Noise filtering capacity: Denoised Lorenz outputs (red) reconstructed from noisy inputs (blue) at SD from 0.01 to 1.0.

i, Comparative denoising performance: Mean squared error (MSE) of reconstructed Lorenz signals across network architectures (TIN reservoir vs shuffled TIN, RNN, LSTM, GRU). TIN achieved minimal MSE.

j, 3D morphological reconstruction: Lorenz attractor morphology recovery under SD=0.1 noise. TIN reservoir (red) outperformed artificial networks in trajectory preservation.

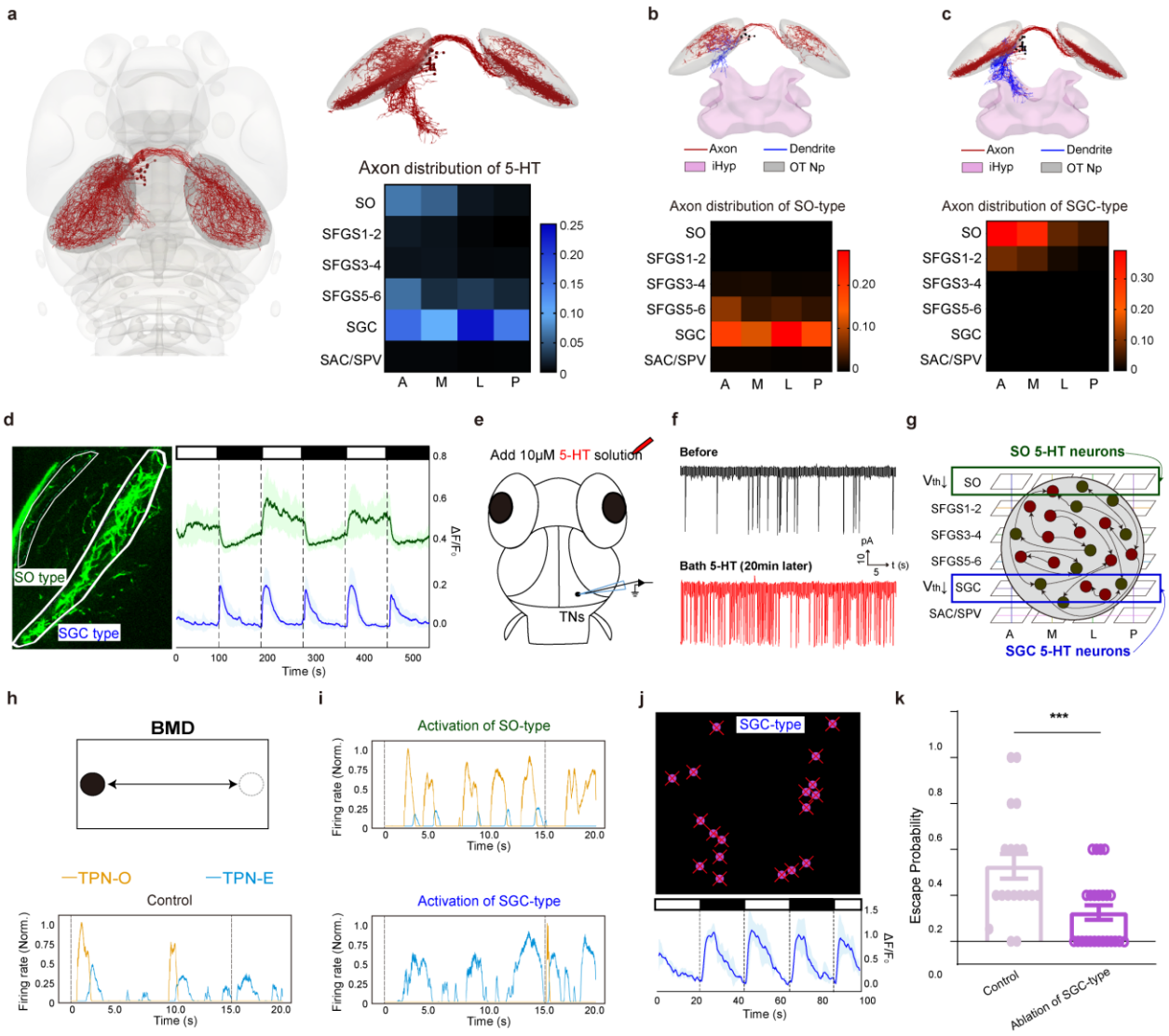

Fig. 4. 5-HT systems endow the TIN reservoir with flexibility for visual processing.

a, Spatial distribution of 5-HT across 24 OT Np microdomains.

b,c, Serotonergic neurons are divided into two types based on innervated in neuropil: SO-Type axons concentrated in superficial layers (b), while SGC-Type axons dominated deeper strata (c) (z-score normalized axonal density).

d, Light-response dichotomy in 5-HT subtypes: SO-Type 5-HTergic neurons exhibited sustained ON responses (tonic firing during illumination), whereas SGC-Type neurons showed transient ON-OFF responses (phasic bursts at light transitions).

e, In vitro modulation assay: Whole-cell patch-clamp recording during 5-HT bath application (10 μM, 5 min) in TNs.

831 **f,g** (f) Spontaneous firing increased post-5-HT and (g) Proposed mechanism: 5-HT lowers
832 activation thresholds of layer-specific TINs (schematic).
833 **h,i** Pathway-specific gain control: Under BMD stimuli, (h) control: balanced TPN-E/O firing; (i)
834 SO-Type 5-HT photo-stimulation biased responses to TPN-O (orienting), while SGC-Type 5-HT
835 enhanced TPN-E (escape).
836 **j,** Optogenetic lesion of SGC-Type 5-HT neurons identified by photo-response screening.
837 **k,** SGC-Type 5-HT lesions reduced looming-triggered escape probability.

Extended Data Figures

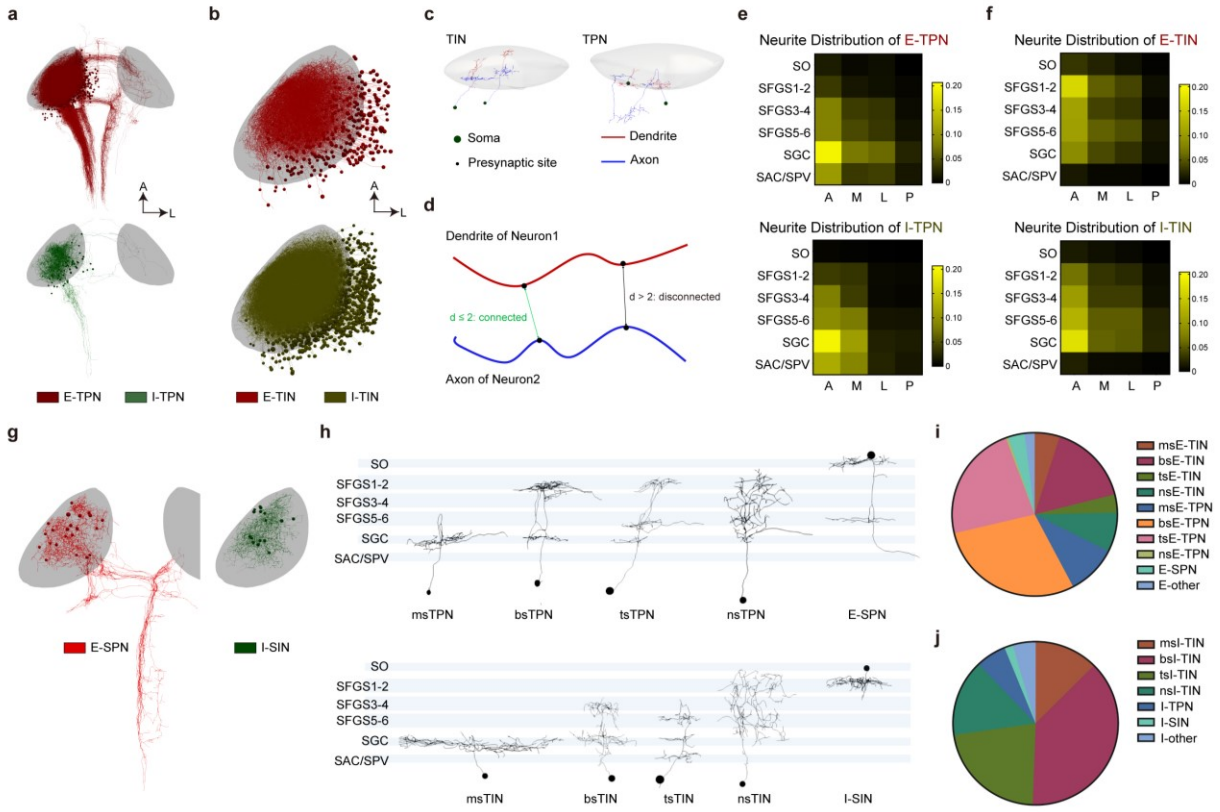

Extended Data Fig. 1. Multidimensional characterization of TNs.

a,b Excitatory-inhibitory (E-I) anatomical organization of (a) TPN and (b) TIN subtypes. Including 348 excitatory TPNs (E-TPNs), 57 inhibitory TPNs (I-TPNs), 180 excitatory TINs (E-TINs), and 845 inhibitory TINs (I-TINs) from zebrafish mesoscopic connectome.

c, Axo-dendritic morphological differentiation of TINs and TPNs. Synaptic release sites were labeled by crossing with *Tg(UAS:sypb-APEX2-TagRFP)* zebrafish, where presynaptic compartments (TagRFP^{+} puncta) defined axonal territories, and dendritic domains were identified by the absence of TagRFP signal.

d, Schematic of neuronal connectivity quantification. Putative connections were defined by axodendritic appositions within ≤2 voxel distances (3 um isotropic resolution). Connection weights (edge thickness) were proportionally scaled to the number of contiguous voxel appositions between axonal terminals and dendritic arbors.

853

854 **e,f** Excitatory-inhibitory neurite distribution in (c) TPNs and (d) TINs. Heatmap of normalized
855 total neurite length across OT Np microdomains. All neurite lengths were normalized to the
856 maximum value per subtype (0–1 scale).
857 **g,** Excitatory projection neurons (E-SPN) and inhibitory superficial interneurons (I-SIN) with
858 soma located in the neuropil.
859 **h,** Laminar classification of OT neurons by stratification and projection. Upper: Extratectal
860 projection neurons - monostratified TPN, msTPNs; bistratified TPN, bsTPN; tristratified TPN,
861 tsTPN; non-stratified TPN, nsTPNs; excitatory superficial projection neuron, E-SPN. Lower:
862 tectal interneurons with stratification - monostratified TIN, msTIN; bistratified TIN, bsTIN;
863 tristratified TIN, tsTIN; non-stratified TINs nsTIN; inhibitory superficial interneuron, I-SIN.
864 **i,j,** Pie charts quantifying morphological diversity of (g) excitatory and (h) inhibitory TNs.
865 Excitatory subtypes: msE-TIN (4.93%), bsE-TIN (16.14%), tsE-TIN (3.59%), nsE-TIN (7.77%),
866 msE-TPN (9.87%), bsE-TPN (29.00%), tsE-TPN (23.02%), nsE-TPN (0.45%), E-SPN (3.29%),
867 E-other types (1.94%) (n=561 cells). Inhibitory subtypes: msI-TIN (12.49%), bsI-TIN (38.09%),
868 tsI-TIN (22.16%), nsI-TIN (15.19%), I-TPN (5.93%), I-SIN (1.66%), I-other types (4.47%)
869 (n=961 cells).
870

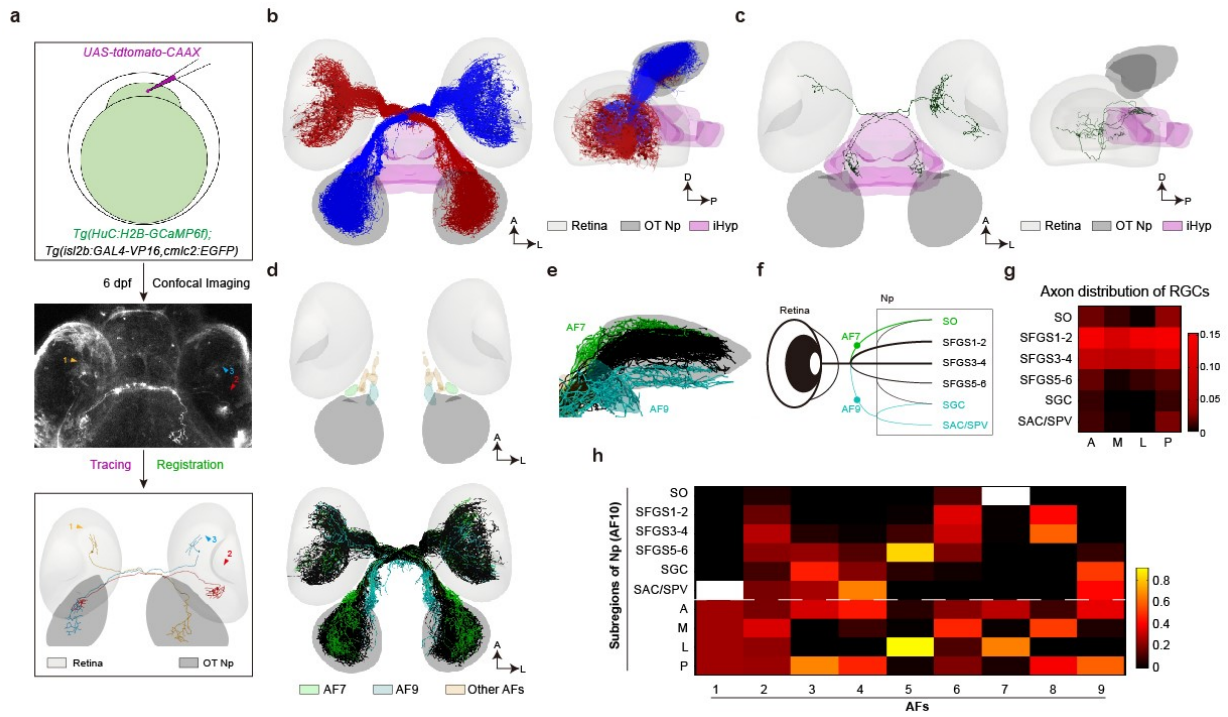

Extended Data Fig. 2. Topographic projections of RGCs.

a, Schematic diagram illustrating the workflow for acquiring single-neuron resolution structural data in the zebrafish mesoscopic connectome (Details see Methods).

b,c, Axonal projection targets of RGCs. (b) OT-dominant projections: 99.35% of RGCs innervated contralateral OT Np microdomains. (c) Non-canonical hypothalamic projections: A small subset of RGCs (0.65%) exhibited contralateral projections to the intermediate hypothalamus (iHyp).

d-f, Retinotectal axonal arborization patterns. (d) Delineated AFs in the OT Np (upper) and two distinct axonal trajectories - RGC bundles traversing AF7 to target the SO, and those passing through AF9 projecting to the SAC/SPV (lower). (e) Coronal view of RGC laminar-specific projection architecture within OT Np. (f) Schematic model illustrating retinotopic-laminar convergence principles.

g, Population-wide RGC projection density heatmap across OT microdomains. Axonal arborization patterns were visualized by normalizing total axonal length projections to maximum intensity (0–1 scale).

887 **h,** Quantitative mapping of AF-specific projection distributions. Percentages of RGCs innervating
888 each AF that projected to specific OT Np microdomains. For every AF, the cumulative projection
889 weights along the white dashed lines to six Np layers (stratification axis) and four spatial columns
890 (topography axis) summed to unity.
891

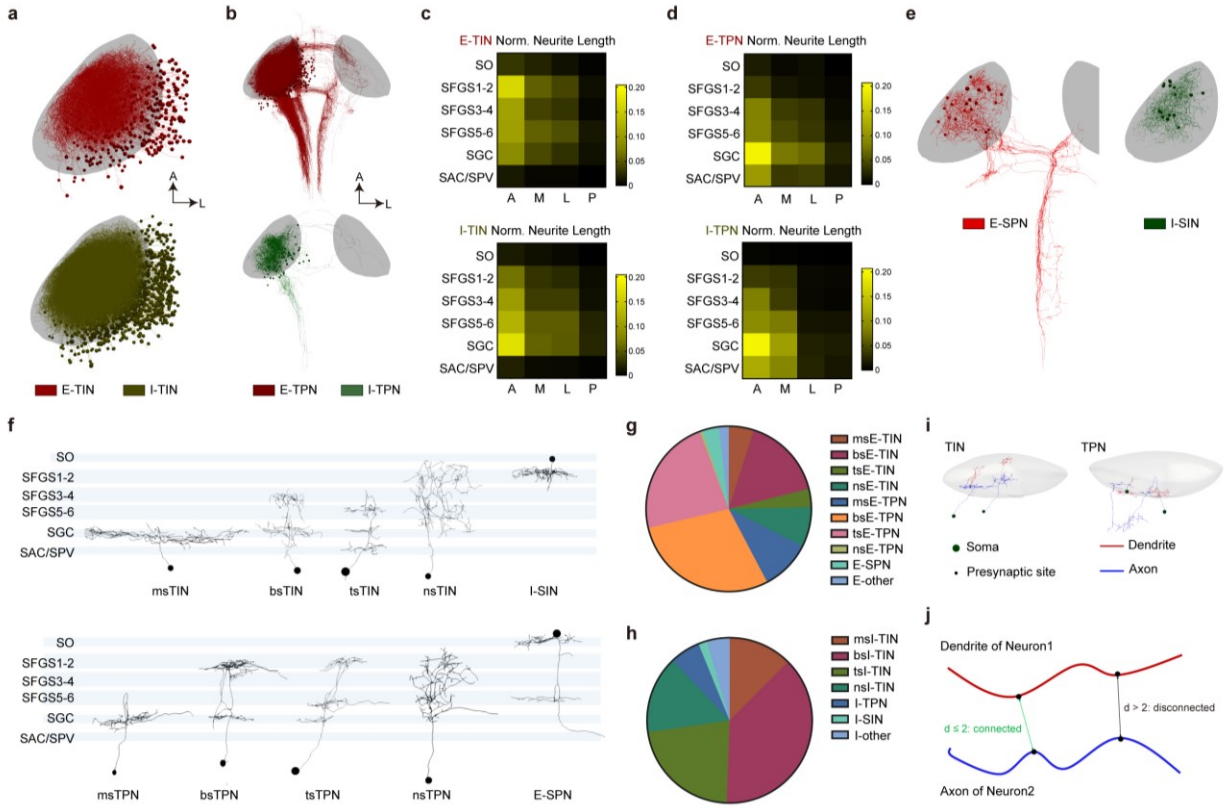

Extended Data Fig. 3. Multidimensional characterization of TNs.

a,b Excitatory-inhibitory (E-I) anatomical organization of (a) TIN and (b) TPN subtypes.

c,d Excitatory-inhibitory neurite distribution in (c) TINs and (d) TPNs. Heatmap of normalized total neurite length across OT Np microdomains. All neurite lengths were normalized to the maximum value per subtype (0–1 scale).

e, Morphological segregation of excitatory projection neurons (E-SPN) and inhibitory superficial interneurons (I-SIN).

f, Laminar classification of OT neurons by stratification and projection. Upper: tectal interneurons with stratification - monostratified TIN, msTIN; bistratified TIN, bsTIN; tristratified TIN, tsTIN; non-stratified TINs nsTIN; inhibitory superficial interneuron, I-SIN. Lower: Extratectal projection neurons - monostratified TPN, msTPNs; bistratified TPN, bsTPN; tristratified TPN, tsTPN; non-stratified TPN, nsTPNs; excitatory superficial projection neuron, E-SPN.

g,h, Pie charts quantifying morphological diversity of (g) excitatory and (h) inhibitory TNs. Excitatory subtypes: msE-TIN (4.93%), bsE-TIN (16.14%), tsE-TIN (3.59%), nsE-TIN (7.77%), msE-TPN (9.87%), bsE-TPN (29.00%), tsE-TPN (23.02%), nsE-TPN (0.45%), E-SPN (3.29%),

908 E-other types (1.94%) (n=561 cells). Inhibitory subtypes: msI-TIN (12.49%), bsI-TIN (38.09%),
909 tsI-TIN (22.16%), nsI-TIN (15.19%), I-TPN (5.93%), I-SIN (1.66%), I-other types (4.47%)
910 (n=961 cells).
911 **i,** Axo-dendritic morphological differentiation of TINs and TPNs. Synaptic release sites were
912 labeled by crossing with *Tg(UAS:sypb-APEX2-TagRFP)* zebrafish, where presynaptic
913 compartments ($TagRFP^+$ puncta) defined axonal territories, and dendritic domains were identified
914 by the absence of TagRFP signal.
915 **j,** Schematic of neuronal connectivity quantification. Putative connections were defined by
916 axodendritic appositions within ≤2 voxel distances (3 um isotropic resolution). Connection
917 weights (edge thickness) were proportionally scaled to the number of contiguous voxel appositions
918 between axonal terminals and dendritic arbors.

919

920 ## Supplementary tables

921 **Supplementary Table 1. Parameter ranges for LIF neuron models of key cell types.**

	RGCs	All TNs	M-cell	nMLF neurons
τ_m (membrane time constant, ms)	10-20	15–30	15–30	15–25
V_{rest} (resting potential, mV)	-65	-65	-65 to -70	-65
V_{th} (threshold, mV)	-50 to -55	-50 to -55	-50	-50 to -55
V_{reset} (resetting potential, mV)	-65 to -70	-65 to -70	-65 to -70	-65 to -70
R_m (membrane resistance, MΩ)	150–300	150–250	100	150–250
τ_{ref} (refractory period, ms)	2–3	2–5	2–3	2–5

922